UC Berkeley
UC Berkeley Previously Published Works

Title
Barrier-free predictions of short-range ordering/clustering kinetics in binary FCC solid solutions

Authors

Abu-Odeh, Anas
Uberuaga, Blas Pedro
Asta, Mark

Peer reviewed

Barrier-Free Predictions of Short-Range Ordering/Clustering Kinetics in Binary FCC Solid Solutions

Anas Abu-Odeh[a], Blas Pedro Uberuaga[b], Mark Asta[a,c]

[a]*Department of Materials Science and Engineering, University of California, Berkeley, 94720, CA, USA*
[b]*Materials Science and Technology Division, Los Alamos National Laboratory, Los Alamos, 87545, NM, USA*
[c]*Materials Sciences Division, Lawrence Berkeley National Laboratory, Berkeley, 94720, CA, USA*

Abstract

We present comparisons of kinetic Monte Carlo (kMC) simulations of isothermal short-range ordering (SRO) and clustering (SRC) kinetics in binary FCC alloys with a mean-field concentration wave (CW) model. We find that the CW model is able to give order-of-magnitude agreement with kMC simulations for ordering/clustering relaxation times over a wide range of temperatures and compositions. The advantage of the CW model is that it does not require parameterization of vacancy hopping energy barriers, which, for a concentrated alloy, becomes prohibitive. We assess limits in the accuracy of the model, and discuss the effect of cooling rates as well as the extension to multi-component systems. Ultimately, the simplicity and performance of the CW model compared to kMC simulations suggests that it is a useful tool to connect with models of properties dependent on SRO/SRC as well as for designing thermal treatments to control formation of SRO/SRC.

1. Introduction

Short-range ordering (SRO) or clustering (SRC) represent the thermodynamically expected non-random correlations between different chemical species in disordered solid solution alloys. SRO occurs when unlike species attract each other, while SRC occurs when like species attract each other. SRO and SRC have been shown to impact the mechanical properties of solid solution alloys [1–16] as well as their passivation behavior [17, 18]. Models that depend on Warren-Cowley (WC) parameters [19] (α_n), which describe the non-random pair correlations between different chemical species in different neighbor shells (n), are available to calculate the effect of SRO/SRC on diffuse-anti-phase boundary energies [20, 21], stacking fault energies [22], and solute-dislocation interactions [12, 13]. WC parameters at equilibrium are typically calculated from Monte Carlo simulations using energetics based on density-functional theory (DFT) combined with cluster expansions [23], coherent-potential-approximation methods [24], or interatomic potentials [25]. Alternatively, they can be calculated from DFT-based concentration-wave methods [26]. They can also be obtained from experimental diffuse SRO/SRC intensities, although such measurements have been primarily limited to binary alloys.

While it is relatively straightforward to predict equilibrium SRO and SRC states, predicting the kinetics of SRO or SRC formation from some arbitrary starting configuration of

disorder is more difficult. Experimental measurements of relaxation times of the resistivities of disordered binary solid solutions during annealing show a variation of at least four orders of magnitude depending on the system, temperature, and concentration [27–29]. Assuming other microstructural features (e.g., vacancy concentration, dislocation density, grain boundary density, etc.) to remain constant during the annealing process, this change in resistivity is interpreted as a change in SRO or SRC. Such variation in the expected relaxation time of SRO/SRC means that, for an arbitrary solid solution alloy, an isothermal annealing procedure may require a few minutes to a few days before an equilibrium SRO/SRC distribution of solutes is established. Models that can predict the correct timescale for the required annealing to establish a desired SRO/SRC state would be valuable for experimental design as well as for connecting to models that predict SRO/SRC dependent properties.

A brute-force approach to modeling SRO/SRC kinetics would be to run molecular dynamics (MD) simulations using an accurate interatomic potential. An issue with this approach is that a vacancy hop, the dominant diffusion mechanism for metallic alloys not under irradiation, is a rare event on the MD timescale except at high homologous temperatures that may represent a relatively low level of equilibrium SRO/SRC. Thus, the timescale of MD is typically incommensurate with that of ordering/clustering induced by vacancy migration. Additionally, interatomic potential models for alloys that produce the correct equilibrium SRO or SRC distributions and vacancy kinetics are limited in their availability.

An approach alternative to MD is kinetic Monte Carlo (kMC) [30], where the position of a vacancy is evolved stochastically using hop rates that are typically parameterized by harmonic transition state theory (HTST) [31]. kMC simulations allow access to timescales that are orders of magnitude larger than can be accessed from MD, and can use on-lattice models parameterized by DFT calculations [32–34]. However, there are typically on the order of ten to one hundred DFT-calculated transition state energies for vacancy hops used for parameterization in such models due to their limiting computational cost. Neural network models that predict a local configuration dependent energy barrier for a vacancy hop need to be trained on the order of 10^3-10^4 energy barriers to achieve accuracy near 10 meV as evidenced by studies using interatomic potentials [35, 36]. Such a number of energy barriers is computationally expensive to obtain from more realistic DFT calculations, as implied by the comparison of a recently developed neural network interatomic potential for CrCoNi to only 100 DFT calculated barriers [37]. Thus, the generation of a reliable on-lattice model for kMC is not trivial. We note that on-the-fly kMC using an interatomic potential can be used to model SRO/SRC kinetics, but this is likely much more computationally expensive than an on-lattice model (in addition to being dependent on the quality of the interatomic potential) and to our knowledge has so far only been attempted for a model Lennard-Jones system [38].

An alternative approach to modeling SRO/SRC kinetics would be to use mean-field or rate-theory models. Examples of such models include the path-probability method, which has been used to study order-disorder transformations [39] and long-range order relaxation [40], as well as rate theories that consider the effect of the change of pair probabilities on the vacancy energy barriers [41–44]. The main issue with these approaches is that they are only tractable when considering a limited range of atom-atom and vacancy-atom interactions. A mean-field model that does not suffer from this issue is the reciprocal-space concentration-wave (CW) formalism, as described for example by Cook and de Fontaine

2

[45–49] and Khachaturyan [50]. In contrast to the previously mentioned models, which focus on correlations in real space, the CW model focuses on describing the change in the Fourier transform of the WC SRO parameters $(\alpha(\vec{k}))$ over time as a function of the concentration-wave wavevector $(\vec{k})$. Advantages of this model are that it does not require any parameterization of vacancy-atom interactions or configuration-dependent energy barriers, and can handle arbitrarily long range atom-atom interactions, although a kinetic mobility term is required that can be related to experimentally measured bulk diffusion constants.

The CW model has shown qualitative and semi-quantitative agreement with experimental measurements of SRO or SRC in binary alloys. It predicts a deviation of the SRO relaxation time from Arrhenius behavior when approaching a critical temperature in agreement with observations from resistivity measurements [27, 46], yields reasonable relaxation times and activation energies for the Au-Ag system when compared to those obtained from resistivity measurements [51], explains why the relaxation of resistivity in a SRC system cannot be explained by a single relaxation time [28], and reasonably describes the exponential kinetics of the SRO diffuse intensity obtained from diffuse scattering experiments in the Cu-Au [52], Cu-Ni [53], and Ni-Fe [54] binary alloys. While these are encouraging results, the previous studies have involved the fitting of at least one input parameter in order to match with experiments, so the predictive capability of the CW model remains unclear. Additionally, the ability for the CW model to describe the kinetics of WC parameter evolution has not been assessed.

In this paper, we present a parameter-free comparison of the kinetics of SRO and SRC formation in models for the ordering and clustering Cu-Au and Cu-Ni systems, respectively, obtained from kMC and the CW model. We find that the relaxation kinetics obtained from the CW model agree with kMC to within an order-of-magnitude for regions in reciprocal space where $\alpha(\vec{k})$ is representative of dominant concentration waves, as well as for real space WC parameters provided the system is at temperatures well above any critical temperatures. This still includes relatively strong SRO and SRC states, as will be discussed below. We also show how the effect of equilibrium vacancy concentrations affect the predictions, as well as discuss how the CW model can be applied to multicomponent systems. The performance of the CW model suggests that it can be used in conjunction with models that use WC parameters as input [12, 13, 20–22] to inform the timescale required for experiments or processing techniques to achieve a desired SRO/SRC-dependent material property.

2. Theory

We first review some details that are necessary for discussion of SRO/SRC kinetics and the CW model. The WC parameter for a neighbor shell n in an AB binary alloy is defined as:

$$\alpha_n = 1 - \frac{P_n(B|A)}{c_B} \tag{1}$$

where $P_n(B|A)$ is the probability of finding a B atom in the nth shell of an A atom, and c_B is the global concentration of B atoms. This can alternatively be written as:

3

$$\alpha_n = \sum_{\vec{r}_n} \alpha_{\vec{r}_n} / Z_n = 1 - \sum_{\vec{r}_n} \frac{P_{\vec{r}_n}(B|A)}{Z_n c_B} \tag{2}$$

where the summation runs over all vectors, $\vec{r}_n$, that connect a central atom to a position in its nth neighbor shell, Z_n is the coordination number for the nth neighbor shell, and $\alpha_{\vec{r}_n}$ and $P_{\vec{r}_n}(B|A)$ are defined for the vector $\vec{r}_n$ instead of the shell n as in Eq. 1. For large, centrosymmetric crystals, the ensemble average of $\alpha_{\vec{r}_n}$ within a shell n should equal α_n. The discrete Fourier transform of all $\alpha_{\vec{r}}$, where $\vec{r}$ is a position in the lattice (including the origin), gives $\alpha(\vec{k})$ at a point $\vec{k}$ in reciprocal space:

$$\alpha(\vec{k}) = \sum_{\vec{r}} \alpha_{\vec{r}} e^{-i2\pi \vec{k} \cdot \vec{r}}. \tag{3}$$

An equivalent and computationally convenient way to represent $\alpha(\vec{k})$ is [46]:

$$\alpha(\vec{k}) = \frac{N|\delta c(\vec{k})|^2}{c_B(1 - c_B)} \tag{4}$$

where N is the total number of atoms in the system, and $\delta c(\vec{k})$ is defined as:

$$\delta c(\vec{k}) = \frac{1}{N} \sum_{\vec{r}} [c(\vec{r}) - c_B] e^{-i2\pi \vec{k} \cdot \vec{r}} \tag{5}$$

where $c(\vec{r})$ takes the value $1(0)$ if the site at position $\vec{r}$ is occupied by a B(A) atom. In this way, $\alpha(\vec{k})$ represents the square amplitude of the concentration wave $\delta c(\vec{k})$ at the $\vec{k}$ wave-vector.

We will summarize the essential results of the CW model, referring interested readers to Refs. [45–49] for details. Starting with a discretized version of Cahn's equation [55] with the inclusion of the effects of thermal fluctuations [56], a solution to the time evolution of $\delta c(\vec{k})$ can be obtained. Through the use of Eq. 4 (as well as some assumptions on the nature of the thermal fluctuations [56]), the kinetics of $\alpha(\vec{k})$ are described as:

$$\alpha(\vec{k}, t) = [\alpha(\vec{k}, 0) - \alpha(\vec{k}, \infty)] e^{-t/\tau(\vec{k})} + \alpha(\vec{k}, \infty) \tag{6}$$

where t is the current time, $\alpha(\vec{k}, 0)$ is the initial value of $\alpha(\vec{k})$, $\alpha(\vec{k}, \infty)$ is the equilibrium value, and $\tau(\vec{k})$ is a $\vec{k}$-dependent relaxation time given by:

$$\tau(\vec{k}) = [2M\beta(\vec{k})\psi(\vec{k})]^{-1}. \tag{7}$$

In Eq. 7, M is a mobility factor related to interdiffusion, $\beta(\vec{k})$ is a geometric factor given by:

$$\beta(\vec{k}) = \sum_{\vec{r}_{nn}} [1 - \cos(\vec{k} \cdot \vec{r}_{nn})] \tag{8}$$

where the sum runs over the unique vectors, $\vec{r}_{nn}$, connecting nearest neighbors, and $\psi(\vec{k})$ is a thermodynamic factor. From fluctuation theory, $\psi(\vec{k})$ can be obtained from knowledge of $\alpha(\vec{k}, \infty)$ [57]:

4

$$\psi(\vec{k}) = \frac{k_B T}{c_B(1 - c_B)\alpha(\vec{k}, \infty)} \tag{9}$$

where k_B is the Boltzmann constant, and T is the temperature.

For a given cubic crystal structure, temperature, and composition of a binary alloy, one needs knowledge of M, $\alpha(\vec{k}, 0)$, and $\alpha(\vec{k}, \infty)$ in order to use Eq. 6. Knowledge of the time evolution of $\alpha(\vec{k}, t)$ at every $\vec{k}$-point allows for an expression of the kinetics of the WC parameters through:

$$\alpha_{\vec{r}_n}(t) = \frac{1}{N} \sum_{\vec{k}}^{BZ} \alpha(\vec{k}, t) e^{i2\pi\vec{k}\cdot\vec{r}_n} \tag{10}$$

where the summation runs over allowable $\vec{k}$-points in the Brillouin zone (BZ).

3. Methods

3.1. On-Lattice Model

As there are many details to the forms and behavior of our on-lattice kMC model, we will give only a brief overview here. Further details on parameterization and fit to reference data can be found in the Supplemental Material (Figures S1-S3).

Interactions between atoms are modeled through a pair-interaction-model (PIM) [58]. The parameters of the PIM are fit to embedded-atom-method (EAM) descriptions of either the face-centered cubic (FCC) Cu-Au [59] or Cu-Ni [60] system. The zero temperature enthalpy of mixing for random alloys at different compositions and the formation energies of ordered structures in Table III of Ref. [58] (excluding the Z1 structure) were evaluated in LAMMPS (Large-scale Atomic/Molecular Massively Parallel Simulator) [61]. Fitting the PIM parameters to this data yielded first and second nearest neighbor interactions that are dependent on the local concentration of the first two neighbor shells around the bonds. To model the change in energy of the system when a vacancy is introduced, we first parameterized nearest neighbor "ghost" interactions between a vacancy and an A or B atom [62]. To improve on this model, we evaluate an effective vacancy formation energy (as defined in Ref. [63]) using 0 K EAM reference data obtained from LAMMPS as well as using the PIM and "ghost" interaction description. The difference between the two energies for a given configuration is then accounted for with a model that includes the global composition and nearest neighbor environment of the vacancy.

Activation energy barriers for vacancy hops are modeled using the concept of a kinetically resolved activation (KRA) barrier [64]. The expression for the energy barrier ($\Delta E_{1\to2}^{act}$) of a vacancy moving from state 1 to state 2 is:

$$\Delta E_{1\to2}^{act} = \Delta E_{1\to2}^{KRA} + \frac{E_2 - E_1}{2} \tag{11}$$

where $\Delta E_{1\to2}^{KRA}$ accounts for the configuration dependent saddle-point contribution to the energy barrier, E_2 is the energy of state 2 and E_1 is the energy of state 1. The configurational dependence of $\Delta E_{1\to2}^{KRA}$ is sampled using climbing image nudged elastic band [65, 66]

calculations of vacancy hop barriers in Cu-Au and Cu-Ni in LAMMPS. A cluster expansion model for $\Delta E_{1 \to 2}^{KRA}$ is fit by considering the configuration of the union of the first nearest neighbor shells of the vacancy and the hopping atom [34] with the model parameters being dependent on global composition.

Attempt frequency quantities are also necessary in order to use HTST. These can be obtained through knowledge of the Hessian of the energy at the minimum and saddle point of a vacancy hop [31]. We have calculated the Hessian of only the diffusing atom in pure Cu, Au, and Ni in LAMMPS at the stable and saddle point. From this, we used concentration and configuration independent attempt frequencies of 3.73 THz, 2.00 THz, 3.65 THz, and 5.64 THz for a vacancy exchange with a Cu atom in the Cu-Au system, a Au atom in the Cu-Au system, a Cu atom in the Cu-Ni system, and a Ni atom in the Cu-Ni system, respectively. The slightly different value for the Cu atom in the two different systems comes from different parameterization of the EAM potentials for pure Cu.

It is important to note that the intention of this is study is not to model the true Cu-Au or Cu-Ni systems, nor is it to accurately replicate the energy landscape of the EAM potentials. Rather, we intend to use the above on-lattice models to represent a physically realistic model for ordering and clustering systems, with vacancy interactions and hopping barriers that are dependent on the local environment (see Supplemental Material).

3.2. Kinetic Monte Carlo Simulations

We start with equilibrium Monte Carlo simulations using a 4,000 atom supercell constructed from a 10x10x10 replication of a conventional FCC unit cell with full periodic boundary conditions. We initially attempt 2×10^7 Monte Carlo swaps in the canonical ensemble across a range of temperatures for Cu-25% Au, Cu-50% Au, Cu-75% Au, and Cu-65% Ni. At low temperature, these compositions are associated with the formation of a (Cu-rich) $L1_2$ ordered phase, a $L1_0$ ordered phase, a (Au-rich) $L1_2$ ordered phase, and the critical composition for phase separation, respectively. We take the variance of the energy of the states obtained from the last 1×10^7 configurations to measure the temperature dependent heat capacity ($C_v(T)$):

$$C_v(T) = \frac{Var[E(T)]}{k_B T^2} \tag{12}$$

where $Var[E(T)]$ is the variance of the energy at temperature T. From the peaks in $C_v(T)$ versus T plots (given in Figure S4 in the Supplemental Material), we estimate that the highest ordering temperature for our model Cu-Au system is 425 K for Cu-50% Au, and the critical temperature for our model Cu-Ni system is between 450-475 K. Thus, in order to model SRO or SRC kinetics, and not long-range ordering or phase separating kinetics, the remaining calculations will be done above those temperatures for Cu-Au and Cu-Ni systems.

To generate non-random states from a desired annealing temperature, we attempted 1×10^6 Monte Carlo swaps in the canonical ensemble starting from a random configuration in order to reach equilibrium SRO/SRC. From a further 1×10^6 attempted swaps, we take 1,000 configurations (one per 1,000 attempted swaps) and find the average values of $\alpha(\vec{k})$ (Eq. 4) across those configurations. This quantity is computed for all $\vec{k}$-points that are commensurate with the periodic vectors of the simulation supercell.

In order to use the CW model, a value for M, the mobility, is required. This can be obtained from dividing the interdiffusion coefficient by the second derivative of the free energy with respect to concentration [45]. For a system where vacancies are treated as a conservative species [67, 68], which will be the case in our kMC simulations, M can be obtained through:

$$M = \frac{\tilde{L}_{AA}\tilde{L}_{BB} - \tilde{L}_{AB}^2}{\tilde{L}_{AA} + \tilde{L}_{BB} + 2\tilde{L}_{AB}} \frac{1}{k_B T} \tag{13}$$

where $\tilde{L}_{ij}$ are kinetic transport coefficients that are related to atomic displacements through [68, 69]:

$$\tilde{L}_{ij} = \frac{(\sum^i \vec{R}(t)) \cdot (\sum^j \vec{R}(t))}{6tN} \tag{14}$$

where $\vec{R}(t)$ is a displacement vector of an atom after a time t and $\sum^i$ represents a sum over all i-type atoms. The $\tilde{L}_{ij}$ coefficients are obtained through kMC simulations, using the methods described below. While M in this study is obtained from kMC, this is only done in order to facilitate a self-consistent comparison of SRO/SRC kinetics from kMC and the CW model for the model systems used in this study. As will be discussed later, for a practical application of the CW model, M is a value to be obtained from experimental interdiffusion data or from mobility databases, circumventing the need to use kMC.

When running kMC, we first replace an atom in the initial state with a vacancy. We then evolve the system in time using the residence time algorithm [30]. The rate (r_q) for each possible vacancy-atom exchange (q) at a kMC step is calculated using HTST:

$$r_q = v_q e^{-\Delta E_q^{act}/(k_B T)} \tag{15}$$

where v_q is an attempt frequency which depends on the type of vacancy-atom exchange. In order to calculate $\tilde{L}_{ij}$ for a given composition and temperature, 1,000 independent kMC simulations, starting from configurations representative of equilibrium SRO/SRC, are carried out for 10,000 kMC steps. $\tilde{L}_{ij}$ for each simulation is then averaged for a given composition and temperature. While tracer diffusivities (which can be related to the kinetic transport coefficients [68]) have been shown to be dependent on the SRO/SRC state [70], we later show in the Discussion section that the evolving SRO/SRC state of our systems does not have a significant effect on the determination of M as we are sufficiently above ordering or critical temperatures.

In order to compare the predictions from the CW model to kMC data, we run 10 independent kMC simulations starting from a non-equilibrium state (which is either a random state or a state annealed at a higher temperature, as discussed below) for $3\text{x}10^6$ kMC steps (except for 600 K in the Cu-Ni system, where we run for $4\text{x}10^6$ kMC steps) while monitoring the first two nearest neighbor WC parameters for a given composition and temperature. For Cu-50% Au at 500 K and Cu-65% Ni at 600 K, we additionally run 100 independent simulations starting from random configurations to provide sufficient statistics to monitor the first eight nearest neighbor WC parameters as well as the change in $\alpha(\vec{k})$. These cases are chosen as they represent the strongest SRO and SRC states, respectively, explored in this study.

7

4. Results

4.1. Equilibrium SRO/SRC

Fig. 1 compares the equilibrium WC parameters obtained from our model Cu-50% Au and Cu-65% Ni systems at 500 K and 600 K, respectively, to those obtained from diffuse scattering experiments of the same systems [71, 72]. Even though the experiments were carried out at higher temperatures, it is clear that our model systems give reasonable WC parameters compared to experimentally observed SRO/SRC. The oscillation of the first eight nearest neighbor WC parameters of the model Cu-50% Au system as well as the positive value of the first four nearest neighbor WC parameters in the Cu-65% Ni system agree with experimental measurments. The first two nearest neighbor WC parameters for other temperatures and compositions are given in Figure S5 in the Supplemental Material.
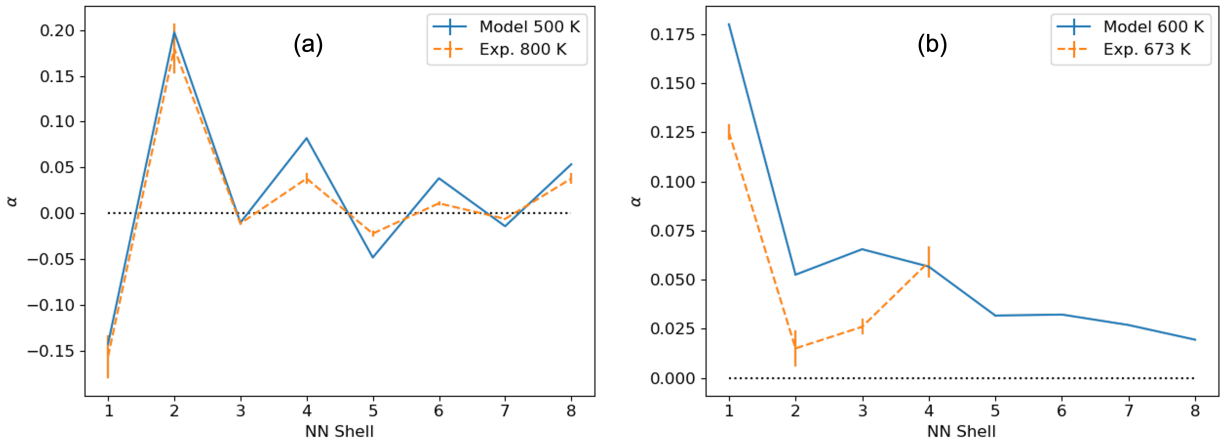

Figure 1: WC parameters measured from the models used in this study compared to those obtained from experiments. (a) Cu-50% Au WC parameters obtained from the model at 500 K and from X-ray diffuse scattering at 800 K [71]. (b) Cu-65% Ni WC parameters obtained from the model at 600 K and from neutron diffuse scattering at 673 K [72]. Error bars for the model values (which are smaller than the thickness of the curves) represent +/- one standard error of the mean, while error bars for the experimental values represent a reported error.

Fig. 2 shows the values of $\alpha(\vec{k})$ along the [100] $\vec{k}$-vector that are expected for random solid solutions, for solid solutions at their equilibrium state, and the average values from initial (random) and final states of kMC runs (after a number of kMC steps mentioned in the previous section for supercells with one vacancy) for Cu-50% Au at 500 K and Cu-65% Ni at 600 K. As expected of the type of SRO/SRC for the studied systems, the equilibrium $\alpha(\vec{k})$ peaks at the [100] position for Cu-50% Au, which represent the enhancement of short-wavelength concentration waves compared to the random state, and peaks near the origin for Cu-65% Ni, which represents the enhancement of long-wavelength concentration waves compared to the random state. The final values of $\alpha(\vec{k})$ from our kMC runs for Cu-50% Au are close to the expected equilibrium values, while the final values of $\alpha(\vec{k})$ from our kMC runs for Cu-65% Ni have not reached the expected equilibrium values. The observed shift in $\vec{k}$-space of the peak of $\alpha(\vec{k})$ in Cu-65% Ni between the final kMC state representing a transient SRC state, and the equilibrium SRC state is an expected behavior of clustering

8

systems [46]. As discussed below, the long relaxation time of this system near the origin of reciprocal space would require much longer kMC simulations to reach equilibrium.
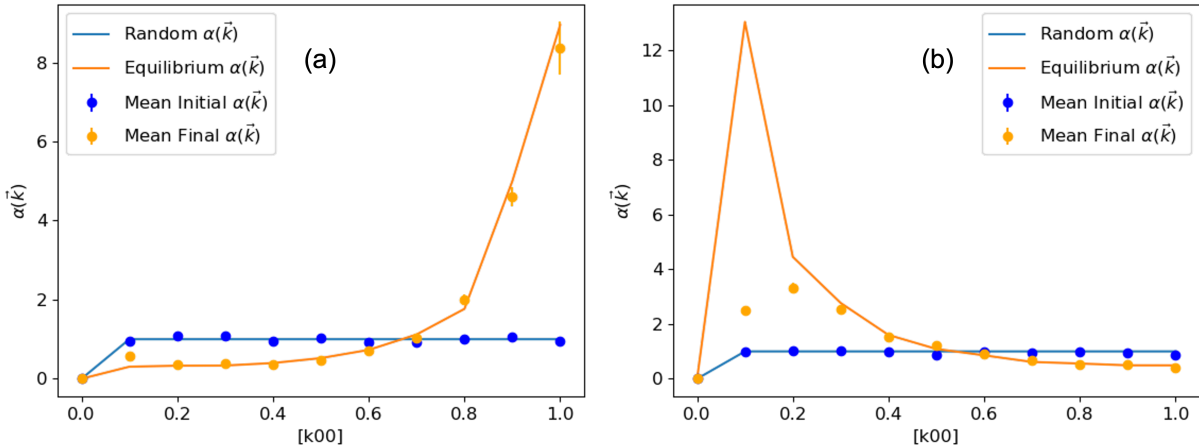

Figure 2: Values of $\alpha(\vec{k})$ along the [100] $\vec{k}$-vector for (a) Cu-50% Au at 500 K and (b) Cu-65% Ni at 600 K. Solid blue lines represent expected values of $\alpha(\vec{k})$ for a random alloy, and solid orange lines represent the equilibrium values of $\alpha(\vec{k})$ as calculated from Monte Carlo in the canonical ensemble. Blue points represent $\alpha(\vec{k})$ averaged over initial random states from kMC runs and orange points represent $\alpha(\vec{k})$ averaged over final states from the same kMC runs. Error bars represent +/- one standard error of the mean.

4.2. Kinetics with a Random Initial State

In this subsection we compare the results of kMC simulations and the CW model predictions of SRO/SRC kinetics starting from a random initial state with one vacancy. As this results in a vacancy concentration that is significantly larger than the equilibrium value, the timescales shown in Figure 3 will be greatly accelerated compared to a realistic vacancy concentration. We will present comparisons to experiments in a later section where we scale the time by an equilibrium vacancy concentration.

Figure 3 shows how the CW model performs in predicting the kinetics of $\alpha(\vec{k})$ relative to kMC. In Figure 3(a) and (b) we compare the inverse relaxation times (or relaxation rates) as predicted by Eq. 7 to those obtained by fitting kMC data to Eq. 6 (representative plots are given in Figure S6 in the Supplemental Material) for Cu-50% Au at 500 K and Cu-65% Ni at 600 K, respectively. For regions where $\alpha(\vec{k})$ is expected to grow compared to the random state (the dominant concentration waves at equilibrium according to Figure 2), the ratio of relaxation rates predicted by the CW model to that obtained from the kMC fits falls into a range of 0.7-2.8 for Cu-50% Au and 0.6-6.1 for Cu-65% Ni. For regions where $\alpha(\vec{k})$ decreases the agreement is worse, and the ratio falls within a range of 2.1-6.9 for Cu-50% Au and 5.5-53.9 for Cu-65% Ni. However, while the ratio of relaxation rates is worse in these regions (i.e., below 1/7[100] for Cu-50% Au, and above 1/5[100] for Cu-65% Ni), the absolute differences in $\alpha(\vec{k})$ are small as shown in Figure 3(c) and (d). As shown in Figure 2, the increase in $\alpha(\vec{k})$ with respect to the random state in the region of dominant concentration waves at equilibrium is larger in magnitude than the decrease associated with the other region in reciprocal space. Interestingly, the CW model tends to predict faster relaxation kinetics than observed through kMC.
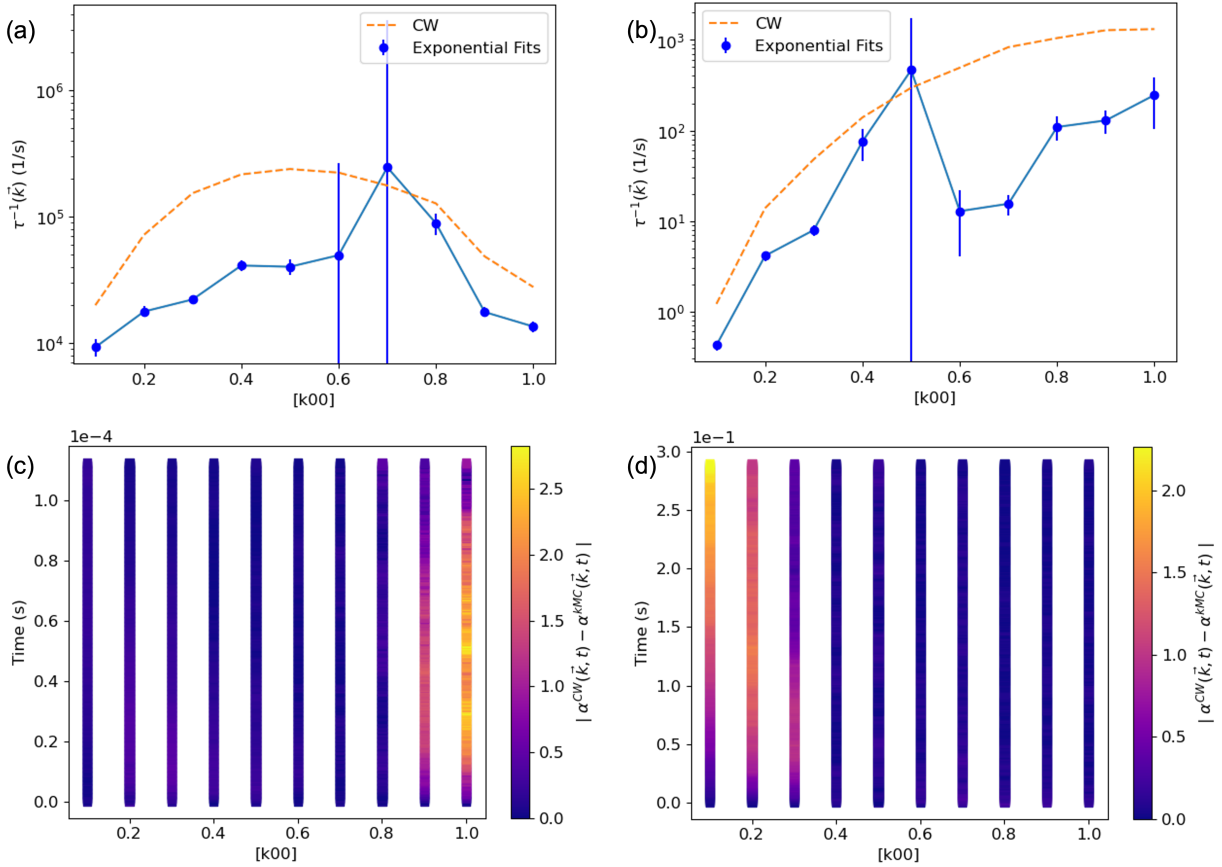
9

Figure 3: Comparison of $\alpha(\vec{k})$ kinetics as predicted by the CW model to kMC results (with one vacancy in the supercell). (a) and (b) show the inverse relaxation time as predicted by the CW model and as fit to kMC data for Cu-50% Au at 500 K and Cu-65% Ni at 600 K, respectively. Error bars represent +/- one standard error on the fits as obtained from bootstrap resampling [73]. (c) and (d) show the absolute difference in $\alpha(\vec{k})$ as predicted by the CW model and as obtained from kMC for Cu-50% Au at 500 K and Cu-65% Ni at 600 K, respectively.

The largest error bars associated with the kMC derived relaxation rates are present at the $1/7[100]$ $\vec{k}$-vector for Cu-50% Au and the $1/5[100]$ $\vec{k}$-vector for Cu-65% Ni. The difference in the initial and final values of $\alpha(\vec{k})$ at these points is very small, and thus the relaxation rate fits to kMC data become extremely sensitive to noise. Additionally, the CW model predicts that the point where $\alpha(\vec{k})$ is equal to one does not change over time, while neutron scattering experiments on Cu-Ni have shown that this is not true [53]. The shifting of this point over time may also lead to a larger error in the fits. It is also worth pointing out that the fits of the CW model to experimental data of neutron scattering in Cu-Ni have significantly better agreement at smaller $\vec{k}$-vectors than larger $\vec{k}$-vectors [53], similar to our results. However, how the errors of the CW model in reciprocal space affect prediction of real-space WC parameters have not, to our knowledge, been explored before this study.

The time dependence of a WC parameter $(\alpha_{\vec{r}_n}(t))$ is related to the time dependence of $\alpha(\vec{k})$ through Eq. 10. To quantify the deviation between the CW model and the kMC

10

results, we have found it useful to introduce a scaling factor C_n defined as:

$$\alpha_n^{kMC}(t) = \alpha_n^{CW}(C_n t) \tag{16}$$

where $\alpha_n^{kMC}(t)$ is obtained from Eq. 1. The value of C_n is derived as that which gives the best agreement between kMC and CW predictions. This quantity then gives the ratio of the timescales of the CW and kMC models to reach a similar value of the WC parameter. If C_n is between 0.1 and 10, then the CW model can reproduce the kinetics of SRO/SRC within an order-of-magnitude of kMC. If C_n equals 1, then the two models have identical timescales for SRO/SRC evolution. As shown below, the value of C_n will depend on alloy concentration, temperature, and initial state. The potential sources for discrepancies between the CW theory predictions and kMC results, as reflected by values of C_n differing from unity, will be given in the Discussion section.

Figure 4 presents a comparison of the kinetics of the WC parameters as obtained from kMC to the CW model. Kinetics for the first four nearest neighbor shells are shown, with plots of the next four nearest neighbor shells given in Figure S7 in the Supplemental Material. The time as obtained from the CW model is scaled by the factors C_n shown in Figure 4(c) for Cu-50% Au at 500 K and Figure 4(d) for Cu-65% Ni at 600 K. The range of C_n is between 0.31 and 0.46 for Cu-50% Au and between 0.17 and 0.33 for Cu-65% Ni. These results thus indicate that the unscaled CW kinetics are within an order-of-magnitude of the kMC results. Similar to the relaxation kinetics in reciprocal space, the CW model seems to predict faster relaxation kinetics in real space compared to kMC as all values of C_n are below 1. Thus, the CW model can be viewed as a lower bound on the true relaxation time scale.

Additionally, the qualitative transient behavior of the WC parameters of the CW model is in excellent agreement with the kMC results. The behavior of the Cu-50% Au WC parameters as shown in Figure 4(a) seem to either monotonically increase or decrease towards their equilibrium values. However, the Cu-65% Ni WC parameters, especially for the second nearest neighbor shell, as shown in Figure 4, show a noticeable non-monotonic behavior, which is captured by both the CW model and the kMC results. It is clear that a simple exponential decay model for the WC parameter kinetics for the SRC system (Cu-Ni) would not satisfactorily capture these effects, consistent with previous findings by Cook [46] and Royen et al. [28]. However, the former study discussed this in terms of the shift of the maximum of $\alpha(\vec{k})$ over time (which is shown in Figure 2(b)), and the latter study uses resistivity relaxation as a proxy to describe SRC relaxation. Through visual inspection of our results, it appears that the WC parameter for the first nearest neighbor shell in a SRC system may be approximated by single exponential kinetics, but this is not true for higher order shells. The WC parameters for the Cu-65% Ni system are further away from their equilibrium values than the Cu-50% Au system, as suggested by the difference in the equilibrium value of $\alpha(\vec{k})$ and the final value obtained from kMC in Figure 2. Compared to the equilibrium value of approximately 0.18, the value of α_1 for the Cu-65% Ni system at the end of the kMC run is approximately 0.15 and still increasing. Based on the relaxation times in Figure 3(b), achieving equilibrium values for the WC parameters would require running 1-2 orders of magnitude more kMC steps due to the slow relaxation of $\alpha(\vec{k})$ near the origin.

While we have been focusing on Cu-50% Au at 500 K and Cu-65% Ni at 600 K due to their relatively strong equilibrium SRO and SRC, we will now explore how the effects of
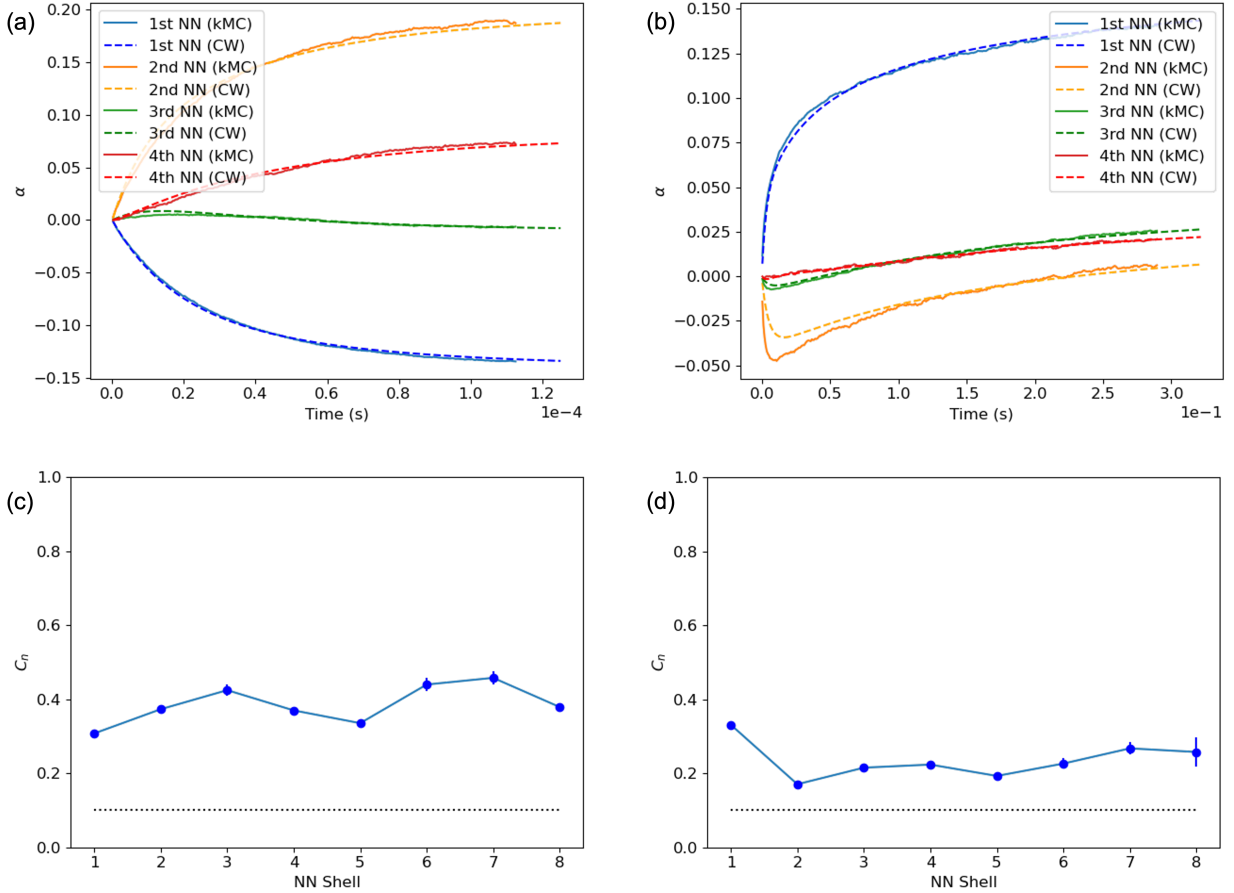
11

Figure 4: Comparison of the kinetics of WC parameters as obtained from kMC and the CW model (with one vacancy in the supercell). (a) and (b) present the time dependence of the WC parameters as given by bin averaging over 100 independent kMC runs (solid lines, +/- one standard error of the mean is present in the form of shaded regions, but are too small to be identified in the plots) and as given by the CW model (dashed lines) for Cu-50% Au at 500 K and Cu-65% Ni at 600 K, respectively. The CW time is scaled by the values of C_n given in (c) for Cu-50% Au and (d) for Cu-65% Ni. Error bars for C_n represent +/- one standard error of the mean as obtained from bootstrap resampling, and the dotted black line marks a value of 0.1.

varied temperature (while maintaining a fixed vacancy concentration) at fixed composition and the effects of varied composition at fixed temperature affect the predictions of the CW model. For the sake of simplicity we focus only on the first two WC parameters. Figure 5 shows the effect of temperature on C_n for Cu-50% Au and Cu-65% Ni for the the first two shells. The general trend shows an increase in C_n with respect to the lowest temperature, although as clearly shown at 1100 K for Cu-65% Ni, the trend is not monotonic. A possible reason for this will be given in the Discussion section. These temperatures represent a range of α_1 (α_2) from -0.14 (0.20) at 500 K to -0.08 (0.08) at 1000 K for Cu-50% Au, and a range of α_1 (α_2) from 0.18 (0.05) at 600 K to 0.08 (-0.01) at 1100 K for Cu-65% Ni. Figure 6 shows the effect on composition on C_n for the Cu-Au system at 500 K and the Cu-Ni system at 600 K for the first two shells. C_n seem to take a range of values, with no clear trend, but are all above 0.1. The two largest errors are associated with the first shell for Cu-10%

Ni and Cu-20% Ni. This is because the values of α_1 for these compositions are very small (-0.004 and 0.01, respectively), so the fit of C_n becomes very sensitive to noise in the data from kMC. Nevertheless, for all the cases observed here, the CW model is able to reproduce SRO and SRC kinetics with timescales within an order-of-magnitude of the kMC results.
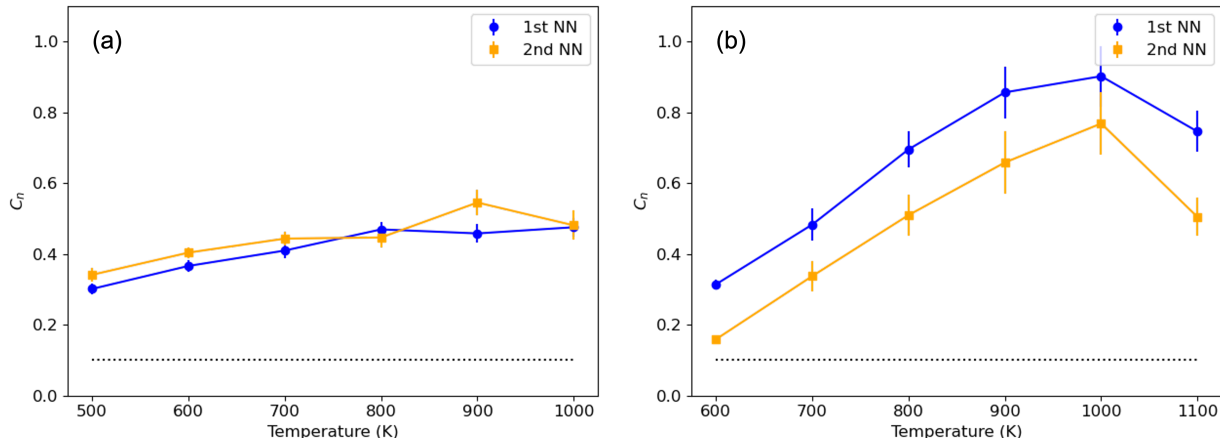

Figure 5: Values of C_n for the first two WC parameters in (a) Cu-50% Au and (b) Cu-65% Ni as a function of temperature. Error bars represent +/- one standard error of the mean as obtained from bootstrap resampling. The black dotted line marks a value of 0.1.
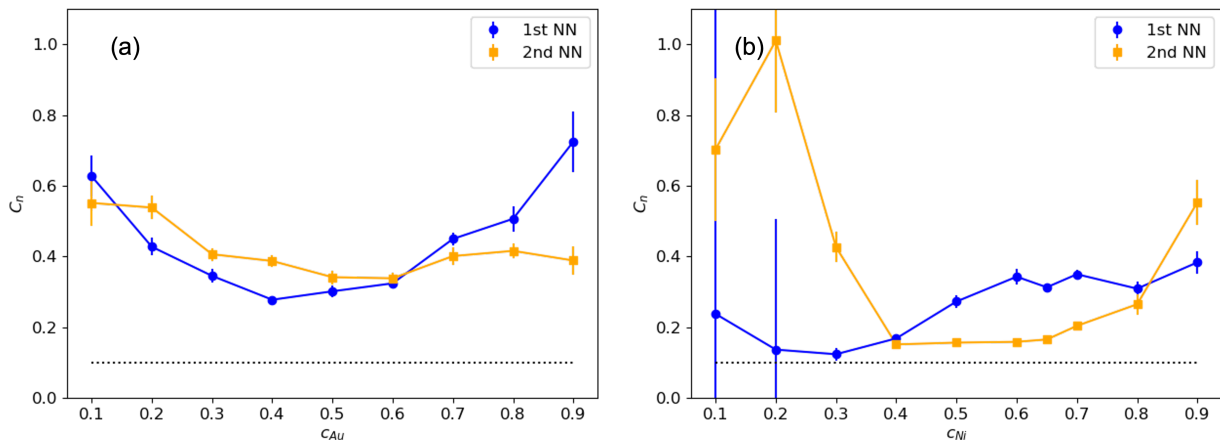

Figure 6: Values of C_n for the first two WC parameters in the (a) Cu-Au system at 500 K and the (b) Cu-Ni system at 600 K as a function of composition. Error bars represent +/- one standard error of the mean as obtained from bootstrap resampling. The black dotted line marks a value of 0.1.

4.3. Non-Random Initial States

The previous results correspond to annealing from an initially random state at a given temperature. In reality, even at very high temperatures, a truly random configuration is not likely as SRO/SRC is always present to some degree. Thus, we have also tested the ability of the CW model to predict SRO/SRC kinetics when quenching in an initial SRO/SRC

13

state from either 400 K or 100 K above the desired annealing temperature. Plots similar to Figure 6 are given for these cases in Figure S8 in the Supplemental Material. Based on the assumptions required in the derivation of the CW model, it would be expected that the closer the initial state is to the equilibrium state, the better the accuracy of the model predictions [46].

As the differences in the initial and equilibrium states are smaller compared to the random case, the fits to Eq. 16 are more sensitive to noise, and thus result in larger error bars for C_n. Regardless, even with the errors, we find that the values of C_n for Cu-Au at 500 K when starting from these non-random initial configurations are closer to 1 than in Figure 6(a), especially for intermediate compositions. This suggests that the CW model gives better predictions for SRO kinetics when the initial state is closer to the equilibrium state.

However, this improvement does not seem to carry over for SRC kinetics for the Cu-Ni system at 600 K. For a couple of cases the prediction from the CW model has become worse than the cases with random initial states presented in Figure 6(b), to the point where there is more than an order-of-magnitude of disagreement with the timescale of the kMC results. A possible reason for this is given in the Discussion section. Comparisons between the CW model and kMC results for SRC relaxation kinetics in Cu-30% Ni when quenching to 600 K from an equilibrium state at 1000 K and in Cu-65% Ni when quenching to 600 K from an equilibrium state at 700 K are given in Figure 7(a) and (b), respectively. The figure shows that there is noticeable deviation between the unscaled ($C_n = 1$) CW model results and the kMC results. To quantify the time-dependent error, we calculate the difference of the predicted WC parameter obtained from the scaled (α_{scaled}^{CW}) and unscaled ($\alpha_{unscaled}^{CW}$) as a function of time. We use the scaled CW model instead of the kMC results as it allows extrapolation to timescales beyond that obtained from kMC. The results are plotted in Figure 7(c) and (d). While the CW model predictions for the cases presented in Figure 7 result in kinetics that are more than an order-of-magnitude faster than kMC results, the expected error for a time-dependent WC parameter is less than 0.02 in magnitude.

4.4. Comparisons to Experiments

The comparisons above represent kinetics of a crystal with a fixed vacancy concentration of 2.5×10^{-4} (i.e. one vacancy in the 4000-atom supercell used for kMC) in the absence of sources and sinks. In order to compare with experimental results, we scale our mobility factors by a calculated equilibrium vacancy concentration, obtained following the procedure in Ref. [74]. The equilibrium vacancy concentrations are given in Figure S9 in the Supplemental Material. The expression for M that is required for Eq. 7 is different than Eq. 13 when considering a non-conserved treatment of vacancies. If we treat vacancies as being regulated by a sufficient amount of sources and sinks to maintain an equilibrium vacancy concentration, the appropriate expression for M is [68]:

$$ M = \left[c_B \left(\frac{\tilde{L}_{AA}}{1 - c_B} - \frac{\tilde{L}_{AB}}{c_B} \right) + (1 - c_B) \left(\frac{\tilde{L}_{BB}}{c_B} - \frac{\tilde{L}_{AB}}{1 - c_B} \right) \right] \frac{c_B(1 - c_B)}{k_B T}. \tag{17} $$

The expressions for M given in Eqs. 13 and 17 are representative of two different limits of vacancy interactions with sinks and sources. Ultimately, how the system behaves will depend heavily on the microstucture, which is sensitive to material preparation and experimental conditions, as well as the relative difference in transport kinetics of the two species [68].
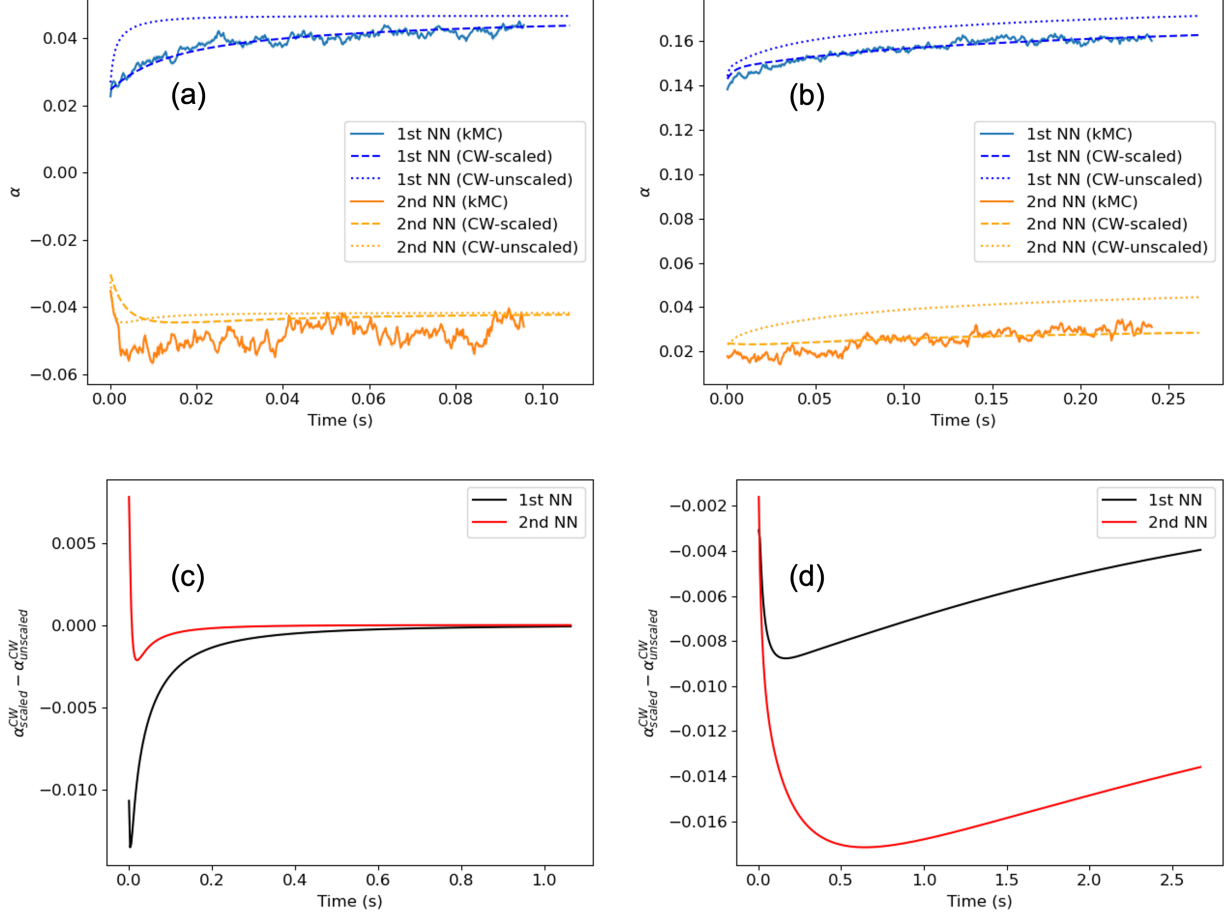
Figure 7: Comparison of the kinetics of WC parameters as obtained from kMC and the CW model (scaled and unscaled) for (a) Cu-30% Ni when quenched to 600 K from 1000 K and (b) Cu-65% Ni when quenched to 600 K from 700 K. Difference between α_{scaled}^{CW} and $\alpha_{unscaled}^{CW}$ as a function of time for (c) Cu-30% Ni when quenched to 600 K from 1000 K and (d) Cu-65% Ni when quenched to 600 K from 700 K.

The latter point is illustrated in Figure S10 in the Supplemental Material. In the following comparisons, we will compare experimental results to predictions from the CW model scaled to equilibrium vacancy concentrations with M calculated using either Eq. 13 or 17.

Figure 8 shows relaxation times calculatd using the CW theory for Cu-50% Au and Cu-65% Ni as a function of temperature. We estimate the relaxation time, τ, for these cases starting with an initially random state as that which satisfies the following equation:

$$\alpha_1^{CW}(t = \tau) = [\alpha_1^{CW}(0) - \alpha_1^{CW}(\infty)]e^{-1} + \alpha_1^{CW}(\infty) \tag{18}$$

where for simplicity $\alpha_1^{CW}(0)$ is set equal to zero. As mentioned above, even at the highest temperatures there is still a notable amount of SRO/SRC at these compositions when equilibrium is reached.

At these high temperatures, the relaxation time for establishing SRO/SRC is much smaller than a second. Thus, after homogenizing a solid solution at a high temperature, the quench rate must be significantly faster than any of the relaxation times at lower tem-

15

peratures to avoid any significant development of SRO/SRC. This is probably difficult to achieve as, even with the slower relaxation times in the Cu-Ni system, a quench rate of approximately 10^4 K/s cannot maintain a SRC state representative of a temperature higher than 973 K for Cu-70% Ni ($\alpha_1 \approx 0.08$) [53]. It is likely even more difficult to suppress the development of SRO in the Cu-Au system, considering the extremely fast relaxation times shown in Figure 8(a).

While there are limited experimental results to compare SRO/SRC kinetics to, Figure 8(b) compares the relaxation times from the CW model to an Arrhenius relation obtained from experimental resistivity measurements [28]. Given the approximations in our on-lattice model, the agreement between experiments and the CW model is reasonable. Since the rate of change of resistivity in the experiments of Cu-Ni cannot be fit to a single exponential, the reported values are associated with an inflection point in the change in resistivity versus the logarithm of time curve.
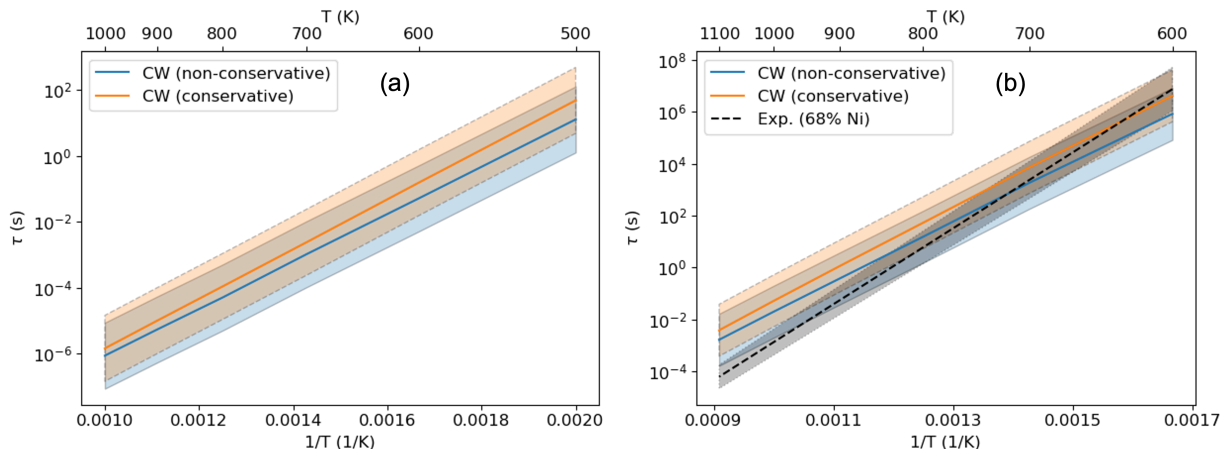

Figure 8: SRO/SRC relaxation times for the first nearest neighbor shell in (a) Cu-50% Au and (b) Cu-65% Ni as a function of temperature as obtained from the CW theory. The shaded blue and orange regions represent +/- an order-of-magnitude from the CW predictions. In (b), the dashed black line represent an Arrhenius relation obtained from experiments [28] near the critical composition and the shaded region represents the reported error in the activation energy.

Figure 9 shows the calculated relaxation times for Cu-Au at 500 K and Cu-Ni at 600 K as a function of composition. The effect of composition can change the relaxation time by orders of magnitude, at least at the temperature considered here. The variation of relaxation time as a function of composition is due to both the compositional dependence of the mobility factor as well as the thermodynamic factor used in Eq. 7. We compare the CW predictions in Figure 9 to relaxation times obtained from resistivity experiments [27, 28, 75]. For Cu-Au, there only seems to be experimental resistivity relaxation times for a couple of Au-rich alloys. At 86% Au [27], an Arrhenius relation, which was fit to data including 500 K, was used to obtain the relaxation time. An Arrhenius relation was not given for 75% Au [75], as relaxation times near this temperature were showing a diverging behavior from an Arrhenius relation while approaching the ordering temperature. Both reported relaxation times are in reasonable agreement (within an order-of-magnitude) with the current predictions.

For Cu-Ni, measurements were made above 600 K and fit to an Arrhenius relation, which

was extrapolated down to 600 K to compare to the current results. The resulting values are in reasonable agreement with the current predictions. However, this should not be taken too literally, as the reported error in the experimental activation energies results in a range of relaxation times that can span many orders of magnitude. Regardless, the CW theory with our current parameterization can reproduce reasonable relaxation times when compared to the limited experimental data. Additionally, while different descriptions of M lead to different predictions of relaxation times, Figs. 8 and 9 show that, at least for our model systems, the different descriptions of M have a secondary effect compared to the effect of temperature and composition.
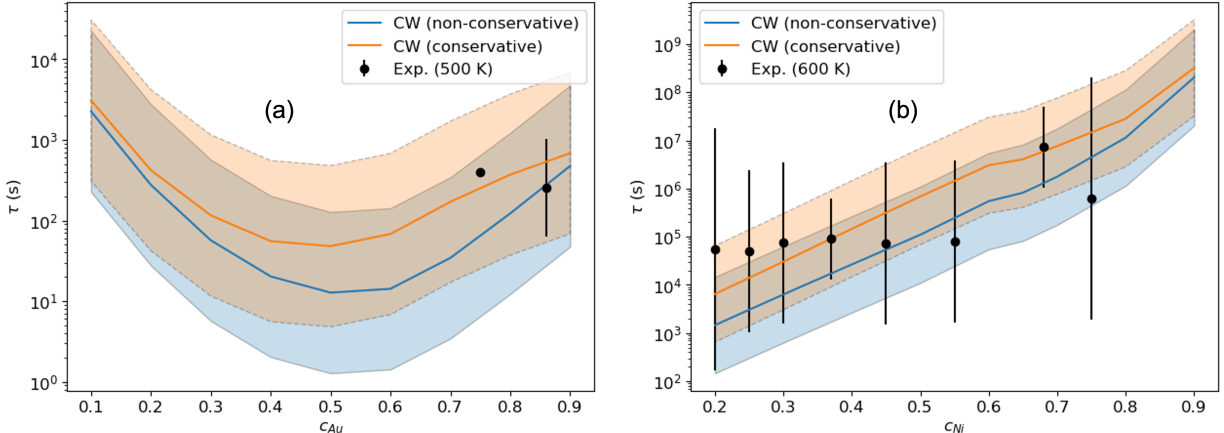

Figure 9: SRO/SRC relaxation times for the first nearest neighbor shell in (a) Cu-Au at 500 K and (b) Cu-Ni at 600 K as a function of composition from the CW theory. The shaded blue and orange regions represent +/- an order-of-magnitude from the CW predictions. Dots with error bars are obtained from Arrhenius relations obtained from experiments [27, 28]. The value at 75% Au in (a) was taken as 400 s without any error bars reported from experiments [75]. As the WC parameter below 20% Ni is very low, relaxation times at lower percents of Ni are not included in (b).

While it is not the goal of this study to replicate the SRO/SRC formation kinetics for the real Cu-Au and Cu-Ni systems, we have compared the interdiffusion coefficient as calculated from our kMC simulations to that obtained from experimentally assessed mobility [76, 77] and thermodynamic data [78, 79]. The comparisons, which are summarized in Figure S11 in the Supplemental Material, provide additional insights into the factors related to the level of agreement between the CW model and experimental relaxation times. For Cu-Au at 500 K, we see in Figure S11(a) that the value of the interdiffusion coefficient agrees well between the experimental data and kMC results when there is more than 70% Au. This agreement suggests that the agreement of the CW model with experimentally obtained relaxation times in Figure 9(a) at 75% and 86% Au is not coincidental. However, with lower concentrations of Au we do not expect the results from our model to describe the true Cu-Au system as the interdiffusion coefficient does not agree between experiments and kMC. For Cu-Ni at 600 K, we see in Figure S11(b) that the interdiffusion coefficient calculated in alloys with less than approximately 49% Ni agrees well between experiments and kMC. Thus it is plausible that despite the large error in relaxation time obtained from the extrapolation of experimental results in Figure 9(b) that the CW model relaxation times could be a reasonable description

of the real system when the concentration is less than 49% Ni. However, Figure S11(b) also shows that above 49% Ni the interdiffusion coefficient between experiments and kMC do not agree well, partly due to the fact that the real Cu-Ni solid solution is expected to be unstable with respect to phase separation in the composition range of 49%-72% Ni at this temperature while our model system is still stable. For Cu-65% Ni, we see in Figure S11(d) that the interdiffusion coefficient determined from experimental data is in good agreement with kMC at low temperatures, but becomes over an order of magnitude larger at higher temperatures. This agrees with the trend in Figure 8(b), where the experimental relaxation times are in good agreement with the CW model at low temperatures, but become over an order of magnitude faster at high temperatures. Thus, given how the agreement between CW model and experimental relaxation times correlates with the agreement between the experimental and kMC interdiffusion coefficient, we believe that the CW model should provide a reasonable description of SRO/SRC formation kinetics in real solid solution systems provided that accurate kinetic and thermodynamic parameters can be obtained.

5. Discussion

5.1. Use in Modeling and Experimental Design

As we have shown above, the CW model is able to capture the same order-of-magnitude timescale of binary SRO/SRC kinetics for a wide range of compositions and temperatures when compared to kMC results. Of course, the temperatures have to be sufficiently larger than ordering ($\sim 1.2 T_{ORD}$) or critical ($\sim 1.3 T_{CRIT}$) temperatures, but they are still representative of relatively high WC parameters near those reported from experiments ($\alpha_1 \approx$ -0.14 for Cu-50% Au and $\alpha_1 \approx 0.18$ for Cu-65% Ni). The CW model requires only two input parameters after defining the initial state: M and $\alpha(\vec{k}, \infty)$. While in this study M was obtained from kMC simulations to be consistent with our on-lattice model, when studying a realistic system M can be obtained from mobility databases such as those used in DICTRA [80] or through simple models based on experimental interdiffusion data [81]. A similar approach is used to parameterize mobility parameters for the Cahn-Hilliard equation in phase-field models [82, 83]. We would expect that a value of M obtained in this way would represent an equilibrium vacancy concentration. $\alpha(\vec{k}, \infty)$ is a quantity that can be obtained from canonical Monte Carlo simulations of the binary system, which does not require the parameterization of any vacancy-atom interactions or vacancy transition state energies. Note that when one is preparing kMC simulations, running canonical or semi-grand canonical Monte Carlo simulations to understand the thermodynamically expected state of the studied system is a necessary step before carrying out any kinetic based study. These simple parameterization steps along with the analytical form of the CW model means that it requires much less effort compared to running kMC simulations.

The time-dependence of the real-space SRO/SRC parameters can be coupled with models of SRO/SRC-dependent material properties to understand the order-of-magnitude timescale at which these properties can change during isothermal annealing. An alternative strategy that may be relevant for design of experiments probing SRO/SRC effects is to look at the predicted relaxation time of dominant concentration waves in reciprocal space as these seem to be in slightly better agreement with kMC than the real-space kinetics (Fig. 3). This is because the real-space kinetics inherits the error of the CW description for all concentration

waves in the Brillouin zone, not just the dominant ones. For systems that exhibit SRO, we would expect that the dominant relaxation time would be associated with the point in reciprocal space that has the maximum value of $\alpha(\vec{k})$ at equilibrium [46]. For systems that exhibit SRC, a dominant relaxation time is difficult to identify as there is a spectrum of relevant relaxation times that continuously increase while moving towards the origin of reciprocal space [46]. However, relaxation times within this spectrum can be used to inform the timescale that long-wavelength compositional fluctuations develop.

5.2. Limitations of the CW Model

While the CW model is a promising tool to predict the timescale for SRO/SRC formation kinetics, there are some limitations. Firstly, the model assumes isothermal kinetics with a fixed concentration of vacancies. Assuming that an experimentally determined M is representative of an equilibrium concentration of vacancies, this means that the CW model can give a lower-bound estimate of the longest waiting time required to reach an SRO/SRC level after quenching from a higher temperature. The waiting time is likely to be reduced if one considers that non-equilibrium vacancy concentrations from higher temperatures are retained for some amount of time and that SRO/SRC formation can occur during the quench [84].

Secondly, the derivation of the CW model begins with the assumption that linear diffusion is valid, which results in treating each concentration wave in reciprocal space as independent. Thus the model does not attempt to conserve the total sum of $\alpha(\vec{k})$ in reciprocal space over time [85], which will result in nonphysical values of $\alpha(\vec{k})$ between the initial and final state. This is likely the origin for disagreement between the model and kMC results at low temperatures where C_n tends to take its lowest values. Additionally, this is likely the source for the initial state dependence of the agreement between the CW model and the kMC results for WC parameter as discussed in Sec. 4.3. This may be alleviated by using a model based on a master equation instead of a linear diffusion equation, although the simplicity of the CW model will be sacrificed [85].

Thirdly, the derivation of the model also assumes that diffusion occurs based on a direct exchange mechanism, as opposed to the much more realistic vacancy exchange mechanism. While this does not seem to pose an issue for ordering systems, for clustering systems at high temperatures and more dilute concentrations, this can result in predicted kinetics, especially at short-wavelengths, that are faster than reality [86]. Evidence for this appears to be present in Fig. 5(b), where the CW model seems to continuously improve its agreement with kMC when increasing the temperature from 600 K to 1000 K (resulting in C_n approaching a value of 1), but begins to deteriorate when further increasing the temperature to 1100 K. We suspect that the better agreement before reaching 1100 K comes from the increased validity of the linear diffusion approximation at higher temperature, but considerations of vacancy-mechanism specific behavior, which can result in heterogeneous kinetic correlations [86], also start to become increasingly important such that the CW prediction at 1100 K has a worse agreement with kMC than at 1000 K. The heterogeneous kinetic correlation effect is expected to be dependent on the magnitude of the value of $\tilde{L}_{AB}$ [86], which we have scaled by Mk_BT and plotted in Figure S12 in the Supplemental Material. Figure S12(d) shows that for the equilibrium state of Cu-65% Ni this value initially decreases as a function

of temperature until 900 K, and then increases. It is this increase at higher temperatures that we suspect contributes to the decrease in C_n at higher temperatures.

Fourthly, M is assumed to be independent of the SRO/SRC state in the CW theory, although it is expected to be dependent on the local concentration inhomogeneity [87]. Additionally, recent MD simulations have suggested that the effect of SRO/SRC will reduce the tracer diffusivities of an alloy [70]. In our implementation of the CW model we used a value of M as obtained at equilibrium. However, for our systems this seems to be a reasonable assumption as the ratio of M obtained at equilibrium to that obtained from a random state ranged from 0.75-1.91 at 500 K for the Cu-Au systems and at 600 K for the Cu-Ni systems (Figure S13 in the Supplemental Material). Interestingly, contrary to the findings in Ref. [70], for concentrated Cu-Au alloys we find that SRO increases the value of M as opposed to decreasing it. This highlights the need for further study of the effect of SRO/SRC on mass transport.

Lastly, the ability to use the CW model for a desired system depends on the availability of interdiffusion experiments or mobility databases relevant to that system. Otherwise, one would have to resort to kMC.

5.3. Extension to Multicomponent Systems

Even with the limitations discussed above, the CW model is a promising tool for understanding SRO/SRC kinetics. The good agreement within the tested compositions and temperatures for our binary systems suggests that this model could be useful for multicomponent systems. In the multicomponent version of the CW model, a system with m components has $m-1$ kinetic equations with an $(m-1)$ by $(m-1)$ matrix of $\vec{k}$-dependent relaxation rates that are related to the product of an $(m-1)$ by $(m-1)$ matrix of mobilities with an $(m-1)$ by $(m-1)$ matrix of $\vec{k}$-dependent thermodynamic factors [48]. Through a diagonalization procedure that obtains the eigenvalues of the relaxation rate matrix and the thermodynamic matrix, one can obtain $m-1$ equations similar to Eq. 6. The mobility matrix can be obtained from experiments or mobility databases, and the thermodynamic matrix can be obtained from canonical Monte Carlo simulations, similar to the binary case. We expect the multicomponent extension of the CW model to be useful for understanding SRO/SRC formation kinetics in complex concentrated alloys and future work to test this theory against kMC simulations are suggested.

6. Conclusions

We have presented comparisons of the mean-field CW model describing SRO/SRC kinetics to results from kMC simulations for two model binary FCC systems. For a wide range of compositions and temperatures, the analytical CW model is able to reproduce the SRO/SRC kinetics from the kMC simulations to within an order-of-magnitude without requiring information of the configurational dependence of vacancy hopping energy barriers nor any adjustable parameters. We also find good agreement in terms of SRO/SRC relaxation times for our systems when compared to available experimental information. This model can be coupled to existing theories that predict SRO/SRC-dependent material properties, and can be extended to multicomponent systems. We expect the CW model to be a valuable tool in aiding the design of thermal processing treatments to control of SRO/SRC states.

Acknowledgements

References

[1] N. Clément, D. Caillard, J. Martin, Heterogeneous deformation of concentrated Ni-Cr F.C.C. alloys: Macroscopic and microscopic behaviour, Acta Metallurgica 32 (6) (1984) 961–975. `doi:10.1016/0001-6160(84)90034-8`.

[2] R. Zhang, S. Zhao, C. Ophus, Y. Deng, S. J. Vachhani, B. Ozdol, R. Traylor, K. C. Bustillo, J. W. Morris, D. C. Chrzan, M. Asta, A. M. Minor, Direct imaging of short-range order and its impact on deformation in Ti-6Al, Science Advances 5 (12) (dec 2019). `doi:10.1126/sciadv.aax2799`.

[3] S. Yin, J. Ding, M. Asta, R. O. Ritchie, Ab initio modeling of the energy landscape for screw dislocations in body-centered cubic high-entropy alloys, npj Computational Materials 6 (1) (2020) 110. `doi:10.1038/s41524-020-00377-5`.

[4] S. Yin, Y. Zuo, A. Abu-Odeh, H. Zheng, X.-G. Li, J. Ding, S. P. Ong, M. Asta, R. O. Ritchie, Atomistic simulations of dislocation mobility in refractory high-entropy alloys and the effect of chemical short-range order, Nature Communications 12 (1) (2021) 4873. `doi:10.1038/s41467-021-25134-0`.

[5] A. Abu-Odeh, M. Asta, Modeling the effect of short-range order on cross-slip in an FCC solid solution, Acta Materialia 226 (2022) 117615. `doi:10.1016/j.actamat.2021.117615`.

[6] A. Abu-Odeh, D. L. Olmsted, M. Asta, Screw dislocation mobility in a face-centered cubic solid solution with short-range order, Scripta Materialia 210 (2022) 114465. `doi:10.1016/j.scriptamat.2021.114465`.

[7] R. Zhang, S. Zhao, J. Ding, Y. Chong, T. Jia, C. Ophus, M. Asta, R. O. Ritchie, A. M. Minor, Short-range order and its impact on the CrCoNi medium-entropy alloy, Nature 581 (7808) (2020) 283–287. `doi:10.1038/s41586-020-2275-z`.

[8] X. Chen, Q. Wang, Z. Cheng, M. Zhu, H. Zhou, P. Jiang, L. Zhou, Q. Xue, F. Yuan, J. Zhu, X. Wu, E. Ma, Direct observation of chemical short-range order in a medium-entropy alloy, Nature 592 (7856) (2021) 712–716. `doi:10.1038/s41586-021-03428-z`.

[9] J. Ding, Q. Yu, M. Asta, R. O. Ritchie, Tunable stacking fault energies by tailoring local chemical order in CrCoNi medium-entropy alloys, Proceedings of the National Academy of Sciences of the United States of America 115 (36) (2018) 8919–8924. doi: 10.1073/pnas.1808660115.

[10] Q. J. Li, H. Sheng, E. Ma, Strengthening in multi-principal element alloys with local-chemical-order roughened dislocation pathways, Nature Communications 10 (1) (2019). doi:10.1038/s41467-019-11464-7.

[11] B. Zhang, J. Ding, E. Ma, Chemical short-range order in body-centered-cubic TiZrHfNb high-entropy alloys, Applied Physics Letters 119 (20) (2021) 201908. doi:10.1063/5.0069417.

[12] E. Antillon, C. Woodward, S. Rao, B. Akdim, T. Parthasarathy, Chemical short range order strengthening in a model FCC high entropy alloy, Acta Materialia 190 (2020) 29–42. doi:10.1016/j.actamat.2020.02.041.

[13] E. Antillon, C. Woodward, S. Rao, B. Akdim, Chemical short range order strengthening in BCC complex concentrated alloys, Acta Materialia 215 (2021) 117012. doi:10.1016/j.actamat.2021.117012.

[14] W.-R. Jian, Z. Xie, S. Xu, Y. Su, X. Yao, I. J. Beyerlein, Effects of lattice distortion and chemical short-range order on the mechanisms of deformation in medium entropy alloy CoCrNi, Acta Materialia 199 (2020) 352–369. doi:10.1016/j.actamat.2020.08.044.

[15] P. Yu, J.-p. Du, S. Shinzato, F.-s. Meng, S. Ogata, Theory of history-dependent multi-layer generalized stacking fault energy— A modeling of the micro-substructure evolution kinetics in chemically ordered medium-entropy alloys, Acta Materialia 224 (2022) 117504. doi:10.1016/j.actamat.2021.117504.

[16] M. Zhang, Q. Yu, C. Frey, F. Walsh, M. I. Payne, P. Kumar, D. Liu, T. M. Pollock, M. D. Asta, R. O. Ritchie, A. M. Minor, Determination of peak ordering in the CrCoNi medium-entropy alloy via nanoindentation, Acta Materialia (2022) 118380doi:10.1016/j.actamat.2022.118380.

[17] M. Liu, A. Aiello, Y. Xie, K. Sieradzki, The Effect of Short-Range Order on Passivation of Fe-Cr Alloys, Journal of The Electrochemical Society 165 (11) (2018) C830–C834. doi:10.1149/2.0871811jes.

[18] Y. Xie, D. M. Artymowicz, P. P. Lopes, A. Aiello, D. Wang, J. L. Hart, E. Anber, M. L. Taheri, H. Zhuang, R. C. Newman, K. Sieradzki, A percolation theory for designing corrosion-resistant alloys, Nature Materials 20 (6) (2021) 789–793. doi:10.1038/s41563-021-00920-9.

[19] J. M. Cowley, An approximate theory of order in alloys, Physical Review 77 (5) (1950) 669–675. doi:10.1103/PhysRev.77.669.

[20] J. Cohen, M. E. Fine, Some aspects of short-range order, Journal de Physique et le Radium 23 (10) (1962) 749–762. doi:10.1051/jphysrad:019620023010074901.

[21] P. Schwander, B. Schönfeld, G. Kostorz, Configurational Energy Change Caused by Slip in Short-Range Ordered Ni–Mo, physica status solidi (b) 172 (1) (1992) 73–85. `doi:10.1002/pssb.2221720109`.

[22] C. R. LaRosa, M. Ghazisaeidi, A "local" stacking fault energy model for concentrated alloys, Acta Materialia 238 (2022) 118165. `doi:10.1016/j.actamat.2022.118165`.

[23] A. van de Walle, M. Asta, First-principles investigation of perfect and diffuse antiphase boundaries in HCP-based Ti-Al alloys, Metallurgical and Materials Transactions A 33 (3) (2002) 735–741. `doi:10.1007/s11661-002-0139-9`.

[24] M. Rahaman, B. Johansson, A. V. Ruban, First-principles study of atomic ordering in fcc Ni-Cr alloys, Physical Review B 89 (6) (2014) 064103. `doi:10.1103/PhysRevB.89.064103`.

[25] S. Ghosh, V. Sotskov, A. V. Shapeev, J. Neugebauer, F. Körmann, Short-range order and phase stability of CrCoNi explored with machine learning potentials, Physical Review Materials 6 (11) (2022) 113804. `doi:10.1103/PhysRevMaterials.6.113804`.

[26] P. Singh, A. V. Smirnov, D. D. Johnson, Atomic short-range order and incipient long-range order in high-entropy alloys, Physical Review B 91 (22) (2015) 224204. `doi:10.1103/PhysRevB.91.224204`.

[27] S. Radelaar, J. M. J. Ritzen, Measurements of the Zener Effect and Kinetics of Short-Range Order in Two Au-Cu Alloys (Containing 14 and 25 at% Cu), physica status solidi (b) 31 (1) (1969) 277–283. `doi:10.1002/pssb.19690310133`.

[28] E. Royen, G. Brandsma, A. Mulder, S. Radelaar, Kinetics of clustering in CuNi-alloys, Scripta Metallurgica 7 (10) (1973) 1125–1128. `doi:10.1016/0036-9748(73)90026-4`.

[29] W. Pfeiler, Investigation of short-range order by electrical resistivity measurement, Acta Metallurgica 36 (9) (1988) 2417–2434. `doi:10.1016/0001-6160(88)90192-7`.

[30] A. F. Voter, Introduction to the kinetic Monte Carlo method, in: Radiation Effects in Solids, Springer Netherlands, Dordrecht, 2007, pp. 1–23. `doi:10.1007/978-1-4020-5295-8_1`.

[31] G. H. Vineyard, Frequency factors and isotope effects in solid state rate processes, Journal of Physics and Chemistry of Solids 3 (1-2) (1957) 121–127. `doi:10.1016/0022-3697(57)90059-8`.

[32] Z. Mao, C. K. Sudbrack, K. E. Yoon, G. Martin, D. N. Seidman, The mechanism of morphogenesis in a phase-separating concentrated multicomponent alloy, Nature Materials 6 (3) (2007) 210–216. `doi:10.1038/nmat1845`.

[33] E. Martínez, O. Senninger, C. C. Fu, F. Soisson, Decomposition kinetics of Fe-Cr solid solutions during thermal aging, Physical Review B - Condensed Matter and Materials Physics 86 (22) (2012) 1–13. `doi:10.1103/PhysRevB.86.224109`.

[34] J. G. Goiri, S. K. Kolli, A. Van der Ven, Role of short- and long-range ordering on diffusion in Ni-Al alloys, Physical Review Materials 3 (9) (2019) 093402. `doi:10.1103/PhysRevMaterials.3.093402`.

[35] B. Xu, J. Zhang, S. Ma, Y. Xiong, S. Huang, J. Kai, S. Zhao, Revealing the crucial role of rough energy landscape on self-diffusion in high-entropy alloys based on machine learning and kinetic Monte Carlo, Acta Materialia 234 (2022) 118051. `doi:10.1016/j.actamat.2022.118051`.

[36] Z. Fan, B. Xing, P. Cao, Predicting path-dependent diffusion barrier spectra in vast compositional space of multi-principal element alloys via convolutional neural networks, Acta Materialia 237 (2022) 118159. `doi:10.1016/j.actamat.2022.118159`.

[37] J.-P. Du, P. Yu, S. Shinzato, F. Meng, Y. Sato, Y. Li, Y. Fan, S. Ogata, Chemical domain structure and its formation kinetics in CrCoNi medium-entropy alloy, Acta Materialia 240 (2022) 118314. `doi:10.1016/j.actamat.2022.118314`.

[38] Z. Shen, J.-p. Du, S. Shinzato, Y. Sato, P. Yu, S. Ogata, Kinetic Monte Carlo simulation framework for chemical short-range order formation kinetics in a multi-principal-element alloy, Computational Materials Science 198 (2021) 110670. `doi:10.1016/j.commatsci.2021.110670`.

[39] H. Sato, R. Kikuchi, Kinetics of order-disorder transformations in alloys, Acta Metallurgica 24 (9) (1976) 797–809. `doi:10.1016/0001-6160(76)90046-8`.

[40] R. Yamada, T. Mohri, Atomistic relaxation process in a Ni3Al ordered phase using path probability method with vacancy mechanisms, Computational Materials Science 167 (May) (2019) 118–122. `doi:10.1016/j.commatsci.2019.05.020`.

[41] M. Schoijet, Theory of the kinetics of short range order, Journal of Physics and Chemistry of Solids 30 (11) (1969) 2571–2588. `doi:10.1016/0022-3697(69)90266-2`.

[42] D. O. Welch, Kinetics of short-range order and Zener relaxation in substitutional solid solutions, Materials Science and Engineering 4 (1) (1969) 9–21. `doi:10.1016/0025-5416(69)90034-2`.

[43] S. Radelaar, On the relation between the relaxation time for short-range order and self-diffusion coefficients, Journal of Physics and Chemistry of Solids 31 (2) (1970) 219–226. `doi:10.1016/0022-3697(70)90102-2`.

[44] G. Yu, K. Lücke, On the theory of short range ordering kinetics under special consideration of correlation effects, Acta Metallurgica et Materialia 40 (10) (1992) 2523–2538. `doi:10.1016/0956-7151(92)90322-6`.

[45] H. Cook, D. De Fontaine, J. Hilliard, A model for diffusion on cubic lattices and its application to the early stages of ordering, Acta Metallurgica 17 (6) (1969) 765–773. `doi:10.1016/0001-6160(69)90083-2`.

[46] H. Cook, The kinetics of clustering and short-range order in stable solid solutions, Journal of Physics and Chemistry of Solids 30 (10) (1969) 2427–2437. `doi:10.1016/0022-3697(69)90067-5`.

[47] D. de Fontaine, H. Cook, Early-stage clustering and ordering kinetics in binary solid solutions, in: Critical Phenomena in Alloys, Magnets, and Superconductors, McGraw-Hill Book Company, 1971, pp. 257–275.

[48] D. de Fontaine, An analysis of clustering and ordering in multicomponent solid solutions—II fluctuations and kinetics, Journal of Physics and Chemistry of Solids 34 (8) (1973) 1285–1304. `doi:10.1016/S0022-3697(73)80026-5`.

[49] D. de Fontaine, Configurational Thermodynamics of Solid Solutions, in: Solid State Physics - Advances in Research and Applications, Vol. 34, Academic Press, Inc., 1979, pp. 73–274. `doi:10.1016/S0081-1947(08)60360-4`.

[50] A. Khachaturian, Theory of structural transformations in solids (1983).

[51] S. Radelaar, The Kinetics of Short-Range Order in Some Ag-Au Alloys, Physica Status Solidi (b) 27 (1) (1968) K63–K67. `doi:10.1002/pssb.19680270164`.

[52] H. Chen, J. B. Cohen, A comparison of experiment and the theory of continuous ordering, Le Journal de Physique Colloques 38 (C7) (1977) C7–314–C7–327. `doi:10.1051/jphyscol:1977762`.

[53] J. Vrijen, J. Aalders, C. Van Dijk, S. Radelaar, Neutron scattering study on the kinetics of clustering in CuNi alloys, Physical Review B 22 (4) (1980) 1503–1514. `doi:10.1103/PhysRevB.22.1503`.

[54] F. Bley, Z. Amilius, S. Lefebvre, Wave vector dependent kinetics of short-range ordering in 62Ni0.765Fe0.235, studied by neutron diffuse scattering, Acta Metallurgica 36 (7) (1988) 1643–1652. `doi:10.1016/0001-6160(88)90231-3`.

[55] J. W. Cahn, On spinodal decomposition, Acta Metallurgica 9 (9) (1961) 795–801. `doi:10.1016/0001-6160(61)90182-1`.

[56] H. Cook, Brownian motion in spinodal decomposition, Acta Metallurgica 18 (3) (1970) 297–306. `doi:10.1016/0001-6160(70)90144-6`.

[57] L. Landau, E. Lifshitz, Fluctuations, in: Statistical Physics, Elsevier, 1980, pp. 333–400. `doi:10.1016/B978-0-08-057046-4.50019-1`.

[58] Y. Wang, K. Li, F. Soisson, C. S. Becquart, Combining DFT and CALPHAD for the development of on-lattice interaction models: The case of Fe-Ni system, Physical Review Materials 4 (11) (2020) 113801. `doi:10.1103/PhysRevMaterials.4.113801`.

[59] S. M. Foiles, M. I. Baskes, M. S. Daw, Embedded-atom-method functions for the fcc metals Cu, Ag, Au, Ni, Pd, Pt, and their alloys, Physical Review B 33 (12) (1986) 7983–7991. `doi:10.1103/PhysRevB.33.7983`.

[60] S. M. Foiles, Calculation of the surface segregation of Ni-Cu alloys with the use of the embedded-atom method, Physical Review B 32 (12) (1985) 7685–7693. `doi:10.1103/PhysRevB.32.7685`.

[61] S. Plimpton, Fast Parallel Algorithms for Short-Range Molecular Dynamics, Journal of Computational Physics 117 (1) (1995) 1–19. `doi:10.1006/jcph.1995.1039`.

[62] M. Doyama, J. Koehler, The relation between the formation energy of a vacancy and the nearest neighbor interactions in pure metals and liquid metals, Acta Metallurgica 24 (9) (1976) 871–879. `doi:10.1016/0001-6160(76)90055-9`.

[63] A. Van der Ven, G. Ceder, Vacancies in ordered and disordered binary alloys treated with the cluster expansion, Physical Review B 71 (5) (2005) 054102. `doi:10.1103/PhysRevB.71.054102`.

[64] A. Van der Ven, G. Ceder, M. Asta, P. D. Tepesch, First-principles theory of ionic diffusion with nondilute carriers, Physical Review B 64 (18) (2001) 184307. `doi:10.1103/PhysRevB.64.184307`.

[65] G. Henkelman, H. Jónsson, Improved tangent estimate in the nudged elastic band method for finding minimum energy paths and saddle points, The Journal of Chemical Physics 113 (22) (2000) 9978–9985. `doi:10.1063/1.1323224`.

[66] G. Henkelman, B. P. Uberuaga, H. Jónsson, A climbing image nudged elastic band method for finding saddle points and minimum energy paths, The Journal of Chemical Physics 113 (22) (2000) 9901–9904. `doi:10.1063/1.1329672`.

[67] K. W. Kehr, K. Binder, S. M. Reulein, Mobility, interdiffusion, and tracer diffusion in lattice-gas models of two-component alloys, Physical Review B 39 (8) (1989) 4891–4910. `doi:10.1103/PhysRevB.39.4891`.

[68] A. Van der Ven, H.-C. Yu, G. Ceder, K. Thornton, Vacancy mediated substitutional diffusion in binary crystalline solids, Progress in Materials Science 55 (2) (2010) 61–105. `doi:10.1016/j.pmatsci.2009.08.001`.

[69] A. R. Allnatt, A. B. Lidiard, Atomic transport in solids, Cambridge University Press, 2003.

[70] B. Xing, X. Wang, W. J. Bowman, P. Cao, Short-range order localizing diffusion in multi-principal element alloys, Scripta Materialia 210 (2022) 114450. `doi:10.1016/j.scriptamat.2021.114450`.

[71] E. Metcalfe, J. Leake, An X-ray diffuse scattering study of short-range order in CuAu, Acta Metallurgica 23 (9) (1975) 1135–1143. `doi:10.1016/0001-6160(75)90118-2`.

[72] J. Vrijen, S. Radelaar, Clustering in Cu-Ni alloys: A diffuse neutron-scattering study, Physical Review B 17 (2) (1978) 409–421. `doi:10.1103/PhysRevB.17.409`.

[73] B. Efron, Nonparametric estimates of standard error: The jackknife, the bootstrap and other methods, Biometrika 68 (3) (1981) 589–599. `doi:10.1093/biomet/68.3.589`.

[74] A. A. Belak, A. Van der Ven, Effect of disorder on the dilute equilibrium vacancy concentrations of multicomponent crystalline solids, Physical Review B 91 (22) (2015) 224109. `doi:10.1103/PhysRevB.91.224109`.

[75] J. T. Chardon, S. Radelaar, Resistance Measurements of the Kinetics of the Elastic After-Effect in AuCu (75, 25) and AgZn (69, 31), physica status solidi (b) 33 (1) (1969) 439–443. `doi:10.1002/pssb.19690330145`.

[76] J. Wang, H. S. Liu, L. B. Liu, Z. P. Jin, Assessment of diffusion mobilities in FCC Cu-Ni alloys, Calphad: Computer Coupling of Phase Diagrams and Thermochemistry 32 (1) (2008) 94–100. `doi:10.1016/j.calphad.2007.08.001`.

[77] Y. Liu, L. Zhang, D. Yu, Diffusion mobilities in fcc Cu-Au and fcc Cu-Pt alloys, Journal of Phase Equilibria and Diffusion 30 (2) (2009) 136–145. `doi:10.1007/s11669-009-9469-2`.

[78] S. an Mey, Thermodynamic re-evaluation of the CuNi system, Calphad 16 (3) (1992) 255–260. `doi:10.1016/0364-5916(92)90022-P`.

[79] B. Sundman, S. G. Fries, W. Oates, A thermodynamic assessment of the Au-Cu system, Calphad 22 (3) (1998) 335–354. `doi:10.1016/S0364-5916(98)00034-0`.

[80] A. Borgenstam, L. Höglund, J. Ågren, A. Engström, DICTRA, a tool for simulation of diffusional transformations in alloys, Journal of Phase Equilibria 21 (3) (2000) 269–280. `doi:10.1361/105497100770340057`.

[81] W. Zhong, Q. Zhang, J.-C. Zhao, A simple yet general model of binary diffusion coefficients emerged from a comprehensive assessment of 18 binary systems, Acta Materialia 215 (2021) 117077. `doi:10.1016/j.actamat.2021.117077`.

[82] T. Wang, G. Sheng, Z. K. Liu, L. Q. Chen, Coarsening kinetics of γ' precipitates in the Ni-Al-Mo system, Acta Materialia 56 (19) (2008) 5544–5551. `doi:10.1016/j.actamat.2008.07.024`.

[83] W. Wu, U. R. Kattner, C. E. Campbell, J. E. Guyer, P. W. Voorhees, J. A. Warren, O. G. Heinonen, Co-Based superalloy morphology evolution: A phase field study based on experimental thermodynamic and kinetic data, Acta Materialia 233 (2022) 117978. `doi:10.1016/j.actamat.2022.117978`.

[84] J. Andrews, W. Boon, S. Radelaar, Quenched-in disorder as a function of quenching conditions, Physics Letters A 38 (7) (1972) 459–460. `doi:10.1016/0375-9601(72)90767-0`.

[85] H. Yamauchi, D. De Fontaine, Kinetics of order-disorder, in: Order-Disorder Transformations in Alloys, 1974, pp. 148–178.

[86] M. Nastar, Atomic diffusion theory challenging the Cahn-Hilliard method, Physical Review B 90 (14) (2014) 144101. `doi:10.1103/PhysRevB.90.144101`.

[87] G. Martin, Atomic mobility in Cahn's diffusion model, Physical Review B 41 (4) (1990) 2279–2283. `doi:10.1103/PhysRevB.41.2279`.